QUANTUM MEASUREMENT

Quantum sensing with arbitrary frequency resolution

J. M. Boss,* K. S. Cujia,* J. Zopes, C. L. Degen†

Quantum sensing takes advantage of well-controlled quantum systems for performing measurements with high sensitivity and precision. We have implemented a concept for quantum sensing with arbitrary frequency resolution, independent of the qubit probe and limited only by the stability of an external synchronization clock. Our concept makes use of quantum lock-in detection to continuously probe a signal of interest. Using the electronic spin of a single nitrogen-vacancy center in diamond, we demonstrate detection of oscillating magnetic fields with a frequency resolution of 70 microhertz over a megahertz bandwidth. The continuous sampling further guarantees an enhanced sensitivity, reaching a signal-to-noise ratio in excess of 10^4 for a 170-nanotesla test signal measured during a 1-hour interval. Our technique has applications in magnetic resonance spectroscopy, quantum simulation, and sensitive signal detection.

Quantum sensors with new capabilities are driving the field of precision metrology (1, 2). In particular, spin qubits associated with crystal defects in diamond (3) and other materials (4–6) have emerged as highly sensitive probes with nanometer spatial resolution (7, 8). Because the defect spins are well isolated from the environment, they can be controlled with high fidelity, allowing researchers to implement sophisticated quantum manipulation protocols.

A particularly important sensing task is the spectral decomposition of time-varying signals into their frequency components. Quantum metrology employs quantum control techniques to reach this goal. For example, dynamical decoupling methods—originally developed for protecting qubits from decoherence—have been adapted for detecting alternating signals with narrow bandwidth and high signal-to-noise ratio (SNR) (9–11). Other, more recent techniques include dressed-state approaches (12, 13), Floquet spectroscopy (14), and correlative measurements (15). Crucially, the spectral resolution of all of these techniques is limited by the state lifetime of the qubit probe. For nitrogen-vacancy (NV) centers in diamond, reported spectral resolutions are a few hertz at best, even when assisted by a long-lived quantum memory (16).

We introduce a simple concept in which the frequency estimation is solely limited by the stability of an external, classical reference clock and the total available measurement time. Our method takes advantage of the quantum lock-in amplifier (9, 10), which is used to stroboscopically sample the signal of interest. Although the acquired signal is highly undersampled, we show that the original wideband spectrum can be recovered by compressive sampling methods (17). The periodic sampling further guarantees that the SNR increases in proportion to the measurement time. We demonstrate our method by recording signal traces for up to 4 hours, reaching a frequency resolution of 70 μHz and a precision of 260 nHz with SNR > 10^4.

Our experimental demonstration makes use of a spin qubit formed by the negatively charged NV center in diamond. The NV center is a suitable object for our demonstration because it can be efficiently initialized, manipulated, and read out at room temperature by optical and microwave pulses. Furthermore, its sensing technology is well developed (8) and addresses a broad range of potential applications in physics, materials science, and biology (18, 19).

Our approach (Fig. 1) relies on periodic sampling of a signal $x(t)$ in intervals of a sampling period t_s. Each sampling instance consists of three periods, including a quantum lock-in measurement of duration t_a, qubit state readout during t_r, and an additional delay time t_d to accommodate for experimental overhead and adjust the sampling rate. The sampling period is then $t_s = t_a + t_r + t_d$.

To implement the quantum lock-in measurement, we use a Carr-Purcell-Meiboom-Gill (CPMG) decoupling sequence (red pulses in Fig. 1). Specifically, we initialize the qubit to the +X state of
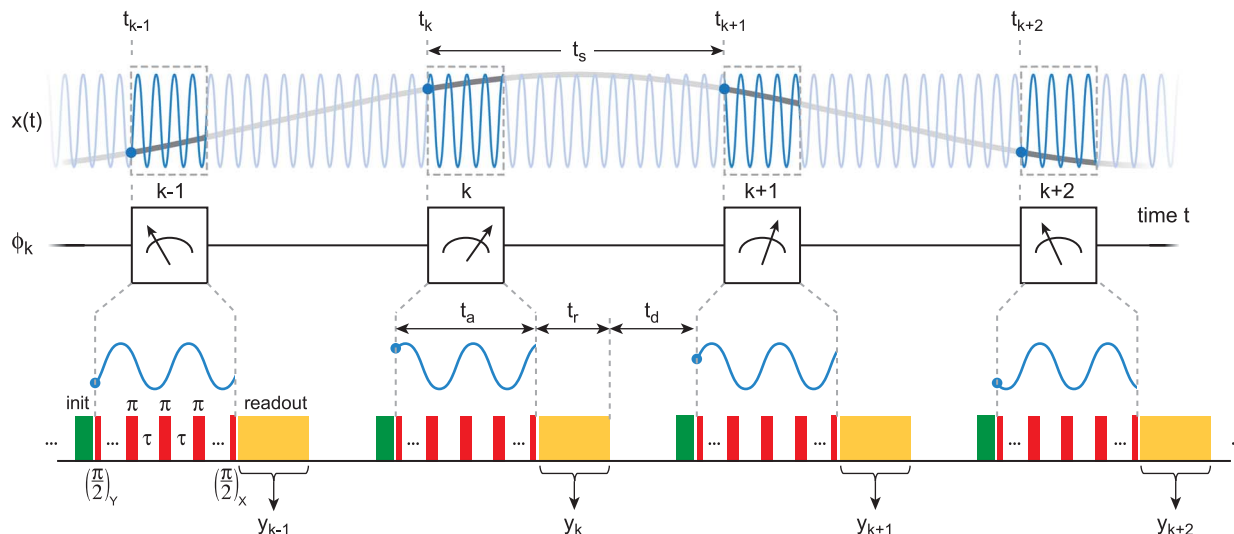
Department of Physics, ETH Zurich, Otto Stern Weg 1, 8093 Zurich, Switzerland.
*These authors contributed equally to this work.
†Corresponding author. Email: degenc@ethz.ch

Fig. 1. Basic concept of continuous sampling. The qubit sensor stroboscopically probes an ac signal $x(t)$ in intervals of the sampling period t_s. Each sampling instance k consists of sensor initialization (green), a phase measurement using quantum lock-in detection (red pulses), and sensor readout (yellow). A sensor output y_k is proportional to the quantum phase ϕ_k and to the instantaneous value of $x(t_k)$ at time stamp t_k (blue dots). A time trace $\{y_k\}$ of sensor outputs therefore contains the undersampled signal $x(t_k)$ (gray oscillation). In our experiment, the sensor qubit was implemented by the electronic spin of a NV center in diamond. A laser pulse was used for initialization and nuclear-spin–assisted optical detection for readout. Quantum lock-in detection was implemented by a CPMG sequence with interpulse spacing τ and either 16 or 32 π pulses (materials and methods) (30).

the *X* basis and modulate it by a series of π pulses with interpulse spacing τ. This defines the lock-in detection frequency $f_{LI} = m/(2\tau)$, where $m = 1,3,5,...$ is the harmonic order. The frequency bandwidth of the lock-in is approximately $f_{LI} \pm 1/(2t_a)$ (*2*, *10*). For an ac signal $x(t) = \Omega\cos(2\pi f_{ac}t)$ with a frequency $f_{ac} \approx f_{LI}$ within this bandwidth, the quantum phase accumulated after time t_a is

$$\phi_k = \frac{2t_a}{\pi}x(t_k) \qquad (1)$$

where t_k marks the start of the lock-in measurement, and Ω is the signal amplitude in units of angular frequency (supplementary text 1). Crucially, although the quantum phase is accumulated over an extended time interval $[t_k, t_k + t_a]$, its value reflects the instantaneous value of $x(t)$ at time $t = t_k$. To read out the quantum phase, the quantum state is measured in the *Y* basis, yielding a probability

$$p_k = \frac{1}{2}(1 - \sin\phi_k) \approx \frac{1}{2}(1 - \phi_k) \qquad (2)$$

to find the system pointing along the −*Y* direction. The approximation is for small $|\phi_k| \ll \pi/2$ within the sensor's linear range (*20*). Optical readout finally converts the projected state into a photon number y_k. Because state projection and optical readout are stochastic processes, y_k is a random variable

$$y_k = \text{Pois}[C(1 - \epsilon\text{Bn}[p_k])] \qquad (3)$$

where Bn is a Bernoulli process, which takes the value 1 with a probability of p_k and the value 0 with probability $1 - p_k$, and Pois is a Poisson process that reflects the photon shot noise. *C* is a variable readout gain and ε is the optical contrast.

By collecting a time trace of *N* measurement outputs $\{y_k\}_{k=1}^{N}$ at sampling times $t_k = kt_s$, we can sample the signal $x(t)$ at a sub-Nyquist rate $f_s = 1/t_s$. Hence, a Fourier transform of the time trace reveals a discrete undersampled spectrum of $x(t)$. Crucially, the number of samples *N* can be made as large as desired, allowing for a frequency resolution $\delta f = f_s/N$ that is arbitrarily fine.

To implement our continuous sampling technique, we used the qubit formed by the $m_S = 0$ and $m_S = -1$ spin sublevels of single NV centers located in diamond nanopillar waveguides (materials and methods). At a bias field of 457 mT applied along the NV symmetry axis, the transition frequency between these states is 9916 MHz. We initialized the qubit using a 532-nm laser pulse and a microwave π/2 pulse and detected the qubit state using a phase-shifted π/2 pulse followed by optical readout. We used an indirect readout scheme in which the final qubit state was first stored in the ^{15}N nuclear spin ($I = 1/2$), serving as a memory qubit, and we then repetitively read out the ^{15}N spin state by a nuclear quantum nondemolition (QND) measurement (*21*, *22*). By varying the number of QND measurements *n*, we could adjust the readout gain *C* between 0 and ~230 photons. The optical contrast was ε ≈ 0.35.

As a first illustration of the continuous sampling technique, Fig. 2, A and B, show a time trace and spectrum of an amplitude-modulated

(AM) magnetic test signal with carrier frequency $f_c = 601.2547$ kHz and modulation frequency $f_{AM} = 10$ mHz. The test signal had an amplitude of ~170 nT, corresponding to $\Omega = 2\pi \times 4.7$ kHz, and was generated by passing an ac current through a nearby wire. The signal contained three components at frequencies f_c and $f_c \pm f_{AM}$, with a power ratio of 1:4:1. The frequency resolution δf of the spectrum, obtained from a time trace of 1-hour duration, was $\delta f = 1/T = 278$ μHz (Fig. 2B, right inset). Because our signal was undersampled, the abscissa in Fig. 2B indicates the detuning from f_c rather than the absolute frequency. The observed microhertz frequency resolution and the consistent amplitude ratio between the carrier

and side peaks illustrate the capabilities of our method.

Though our strategy allows for an arbitrary frequency resolution δf, we are more interested in how precisely we can determine a signal's line-width and center frequency in the experiment. Figure 2C depicts the decrease in the fitted linewidth parameter γ with increasing measurement time *T* for four signals. Signals (i) to (iii) were produced by amplitude modulation, as in Fig. 2B, and had zero intrinsic linewidth, $\gamma_{int} = 0$. The linewidth parameter for these signals scaled with $\gamma \propto T^{-1}$, which represents the Fourier transform limit of the continuous sampling method. The T^{-1} scaling is expected to continue until the
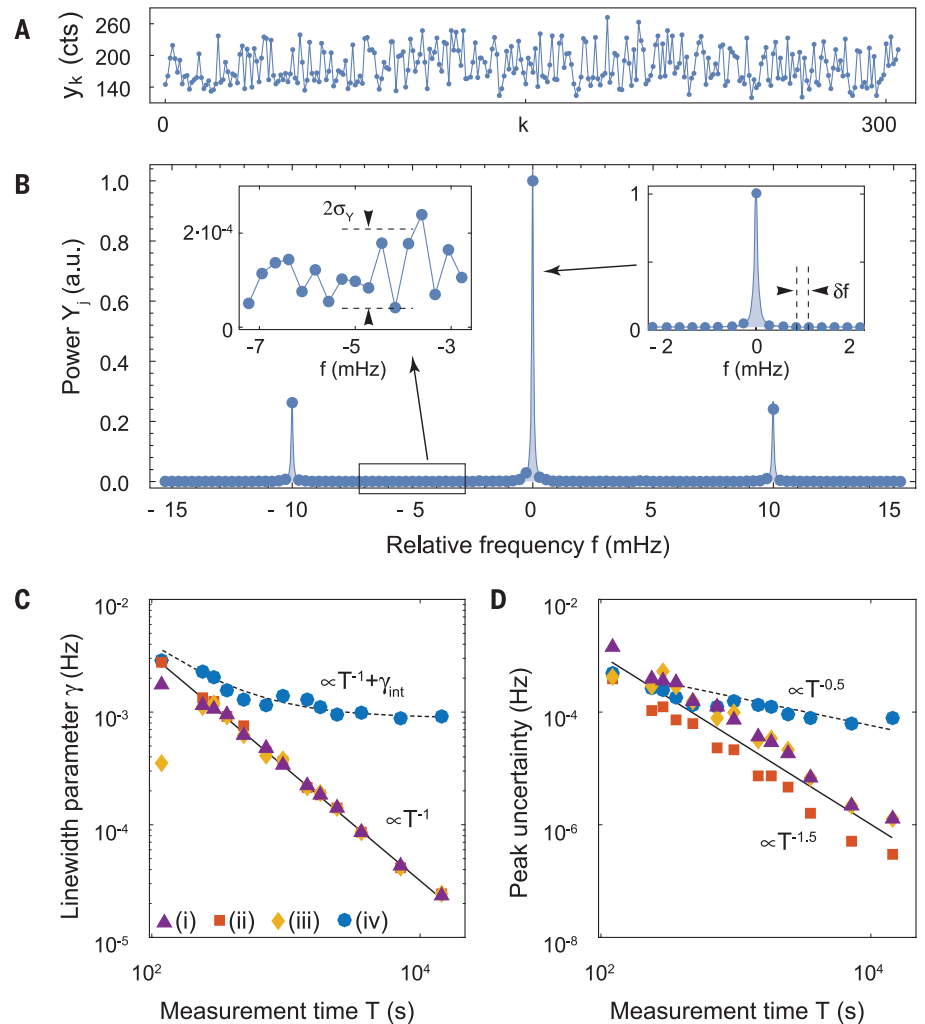

Fig. 2. Continuous sampling of ac magnetic signals. (**A**) A 1.26-s excerpt of a 1-hour time trace sampled at $t_s = 4.2$ ms. The vertical axis shows photon counts. The telegraph-like behavior results from the stochastic quantum state projection. (**B**) Fourier spectrum (power) of the full 1-hour time trace. Three peaks are visible that correspond to the central and side peaks of the amplitude-modulated signal. The horizontal axis indicates the detuning from the carrier frequency. The insets show the noise floor (left inset) and the frequency resolution (right inset) of the spectrum. a.u., arbitrary units. (**C**) Fitted linewidth parameter γ as a function of total measurement time *T* for four signals. Data points (i) to (iii) originate from coherent signals and data points (iv) from an incoherent signal with an artificial line broadening of $\gamma_{int} = 0.76$ mHz. Original spectra are presented in fig. S3. (**D**) Uncertainty in the fitted peak frequencies for the different peaks. Solid and dashed lines are guides to the eye.
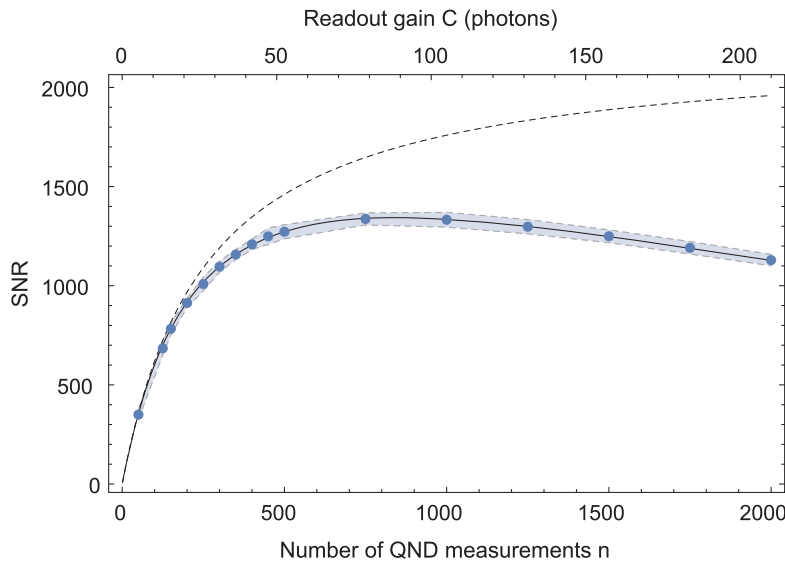
Fig. 3. Signal-to-noise ratio (SNR) as a function of the readout gain C. The readout gain is adjusted via the number of repetitive QND measurements n of the nuclear memory qubit. Blue dots are the experimental data and represent the mean SNR of six time traces with $N = 3.85 \times 10^5$ samples. The dashed line represents the ideal SNR predicted by theory (Eq. 6). The solid line, in addition, takes the depolarization of the nuclear ^{15}N memory qubit into account (supplementary text 3). The filled blue region indicates the standard error of the fit. From our data, we extract a ^{15}N depolarization rate $\Gamma \approx 1.4 \times 10^{-4}$ per readout. The corresponding optimum SNR ($n = 260$) for a 1-hour measurement interval is 1.2×10^4 (materials and methods) (30).
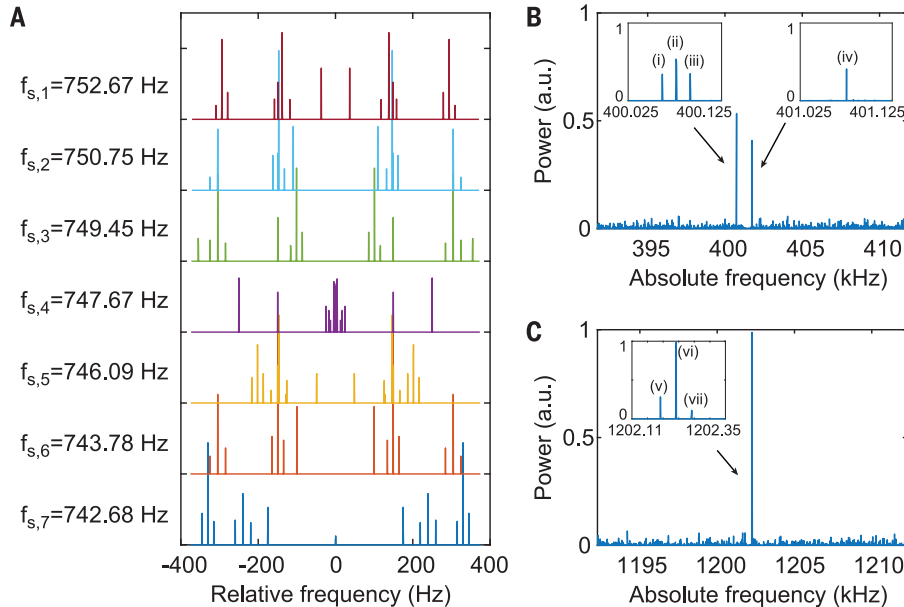

Fig. 4. Wideband spectral reconstruction based on compressive sampling. (**A**) Undersampled spectra obtained from time records with $i = 1,...,7$ random chosen sampling rates $f_{s,i}$. The data represent records of duration $T = 2$ s that were averaged for 1.5 hours. (**B** and **C**) Reconstructed wideband spectrum containing $l = 7$ tones in two subbands. The insets show the individual tones with frequencies $f^{(i)} = f_c - 15$ Hz, $f^{(ii)} = f_c$, $f^{(iii)} = f_c + 15$ Hz, and $f^{(iv)} = f_c + 1000$ Hz (where $f_c = 400.75$ kHz), as well as $f^{(v)} = f'_c - 40$ Hz, $f^{(vi)} = f'_c$, and $f^{(vii)} = f'_c + 40$ Hz (where $f'_c = 1202.25$ kHz). The noise reflects the incomplete image rejection of the reconstruction procedure.

phase noise in the reference clock or the frequency jitter in the signal generator become dominating. Signal (iv), on the other hand, was artificially broadened by frequency modulation with Gaussian noise to mimic a nonzero intrinsic linewidth $\gamma_{int} >$ 0. The linewidth parameter for signal (iv) initially also decreased with the T^{-1} scaling but leveled out as γ approached γ_{int}. Figure 2D further shows the fit errors in the peak frequencies for all signals. Here an observed $T^{-1.5}$ scaling reduced to $T^{-0.5}$

once the intrinsic linewidth became dominating, as expected for the scaling of the spectral amplitude variance (supplementary text 2).

We next examined how the sensitivity of the sensor can be optimized. To quantify the sensitivity, we compared the peak amplitude Y_j with the standard deviation σ_Y of the noise floor in the power spectrum (Fig. 2B). This defines a power SNR

$$SNR = \frac{Y_j}{\sigma_Y} \qquad (4)$$

Assuming that the entire signal power is concentrated in a single Fourier component Y_j of the spectrum (i.e., that the linewidth of the signal is smaller than δf), it follows from Eqs. 2 and 3 that

$$Y_j \approx \frac{1}{16} N^2 C^2 \epsilon^2 \phi_{max}^2 \qquad (5)$$

where $\phi_{max} = 2t_a\Omega/\pi$ is the signal amplitude expressed in units of the accumulated phase (supplementary text 3). The approximation is again for small signals within the linear response of the lock-in (Eq. 2). The noise σ_Y is the sum of two contributions: one from quantum projection noise with variance $\frac{1}{4}NC^2\epsilon^2$ and one from optical shot noise with variance $NC\left(1 - \frac{\epsilon}{2}\right)$. The SNR becomes

$$SNR = \frac{\frac{1}{16}NC^2\epsilon^2\phi_{max}^2}{\frac{1}{4}C^2\epsilon^2 + C\left(1 - \frac{\epsilon}{2}\right)} \qquad (6)$$

Because $N = Tf_s$, the SNR improves proportional to the duration of the time record T.

To further optimize the SNR, we adjusted the phase amplitude ϕ_{max} and the readout gain C. We achieved this by varying the sensing time t_a and the readout time t_r. First, we increased the sensing time t_a so that the quantum phase covered the full linear range of the lock-in, typically ϕ_{max} ~ 0.5. Although larger ϕ_{max} values are possible, the response of the lock-in becomes nonlinear (20), and harmonics are generated in the spectrum. This complicates the interpretation while providing little further improvement in the SNR (supplementary text 1 and figs. S4 and S5). Next, we turned up the gain C until sensor readout became dominated by quantum projection noise. In our experiment, we could adjust C by varying the number n of QND measurements of the nuclear memory qubit, where $C(n) \approx n \times 0.105$ photons and $t_r \approx n \times 2.32$ μs. Figure 3 plots the SNR for signal (ii) in Fig. 2C as a function of n. The SNR increased rapidly for small n until it saturated around $n \approx 260$, which corresponded to the threshold gain $C_{thresh} = 4/\epsilon^2 - 2/\epsilon \approx 27$, where shot noise and quantum projection noise are balanced (2). Increasing the gain beyond C_{thresh} only marginally improved the SNR and eventually even degraded it. The degradation at very high gains was due to the imperfection of the nuclear quantum memory, which became depolarized under optical illumination (22).

Thus far, all of our measurements reported relative rather than absolute signal frequencies. The measurement of absolute signal frequencies is hindered by the large undersampling. For example, in Fig. 2B, a signal of frequency f_c ~ 601 kHz was sampled at $f_s = 0.237$ kHz, which is about

5×10^3 times slower than the Nyquist rate. We now discuss a strategy that makes use of compressive sampling to overcome this limitation. We implemented this strategy by recording a set of time traces with slightly different sampling rates f_s.

Compressive sampling (CS) exploits our prior knowledge about the sparsity of the wideband spectrum (*17*). Suppose the vector $\vec{\mathbf{X}}$ holds the Fourier components of the desired wideband spectrum sampled at or above the Nyquist rate, and the vectors $\vec{\mathbf{Y}}_i$ represent a small set of p undersampled spectra with $i = 1,2,...,p$. We can express our measured undersampled spectra $\vec{Y}_i$ by the linear system

$$\begin{pmatrix} \vec{\mathbf{Y}}_1 \\ \vec{\mathbf{Y}}_2 \\ \vdots \\ \vec{\mathbf{Y}}_p \end{pmatrix} = \begin{pmatrix} \Phi_1 \\ \Phi_2 \\ \vdots \\ \Phi_p \end{pmatrix} \vec{\mathbf{X}} \qquad (7)$$

where Φ_i are sampling matrices folding the wideband spectrum into the bandwidths of the undersampled spectra (*23*). To reconstruct the wideband spectrum, we solve Eq. 7 for $\vec{\mathbf{X}}$. Although the linear system is highly underdetermined, a solution can be found if $\vec{\mathbf{X}}$ is sparse (i.e., if it is substantially nonzero for only a few frequencies) and the Φ_i are mutually incoherent.

To demonstrate wideband spectral reconstruction, we implemented a CS scheme to recover $l = 7$ tones from a set of $p = 7$ undersampled spectra (supplementary text 4). We adjusted the sampling frequencies f_s via the delay time t_d. To ensure incoherence between the sampling matrices, we randomized our choices of t_d. Figure 4 shows the undersampled spectra together with the reconstructed wideband spectrum. The tones in these spectra were contained in two 20-kHz-wide frequency bands, one centered at the first harmonic of the lock-in filter function at 400 kHz and one at the third harmonic at 1200 kHz. Although the SNR of the reconstructed spectrum is reduced because of incomplete image rejection, the experiment clearly demonstrates that the absolute peak fre-

quencies can be unambiguously recovered. The image rejection can be improved by increasing the number of spectra p.

Our experiments demonstrate that a quantum sensor can achieve a frequency resolution far beyond its intrinsic state lifetime, limited only by the stability of an external synchronization clock. Looking forward, quantum sensing with arbitrary frequency resolution has important applications in sensitive magnetic and electric field detection. A high spectral resolution is, for example, essential for nanoscale nuclear magnetic resonance (NMR) imaging experiments (*24, 25*), in which minute spectral shifts can be used to infer atomic positions, internuclear distance vectors, and molecular connectivity. Spectral addressability is also important for operating large-scale quantum registers in solid-state quantum simulators (*26*). Although NMR spectra are often broadened by internuclear interactions, a rich repertoire of line narrowing and isotope dilution techniques exists for refining the spectral resolution (*27, 28*). Ultrahigh-resolution NMR is able to resolve couplings of a few millihertz (*29*) under favorable conditions and achieves <20-Hz linewidths, even for ^{1}H in dense solid samples (*28*). Finally, continuous sampling can provide sensitivity gains when measuring weak, modulated signals. This is because of the high duty cycle achieved by continuously probing the signal during the measurement time T, combined with the favorable $\propto T$ scaling of the SNR.

REFERENCES AND NOTES

1. V. Giovannetti, S. Lloyd, L. Maccone, *Nat. Photonics* **5**, 222–229 (2011).
2. C. L. Degen, F. Reinhard, P. Cappellaro, Quantum sensing. arXiv:1611.02427 [quant-ph] (8 November 2016).
3. M. W. Doherty et al., *Phys. Rep.* **528**, 1–45 (2013).
4. J. J. Pla et al., *Nature* **489**, 541–545 (2012).
5. M. Widmann et al., *Nat. Mater.* **14**, 164–168 (2015).
6. R. Kolesov et al., *Nat. Commun.* **3**, 1029 (2012).
7. G. Balasubramanian et al., *Nature* **455**, 648–651 (2008).
8. P. Maletinsky et al., *Nat. Nanotechnol.* **7**, 320–324 (2012).
9. S. Kotler, N. Akerman, Y. Glickman, A. Keselman, R. Ozeri, *Nature* **473**, 61–65 (2011).
10. G. de Lange, D. Ristè, V. V. Dobrovitski, R. Hanson, *Phys. Rev. Lett.* **106**, 080802 (2011).
11. G. A. Álvarez, D. Suter, *Phys. Rev. Lett.* **107**, 230501 (2011).
12. F. Yan et al., *Nat. Commun.* **4**, 2337 (2013).
13. M. Loretz, T. Rosskopf, C. L. Degen, *Phys. Rev. Lett.* **110**, 017602 (2013).
14. J. E. Lang, R. B. Liu, T. S. Monteiro, *Phys. Rev. X* **5**, 041016 (2015).
15. A. Laraoui et al., *Nat. Commun.* **4**, 1651 (2013).
16. S. Zaiser et al., *Nat. Commun.* **7**, 12279 (2016).
17. D. L. Donoho, *IEEE Trans. Inf. Theory* **52**, 1289–1306 (2006).
18. L. Rondin et al., *Rep. Prog. Phys.* **77**, 056503 (2014).
19. R. Schirhagl, K. Chang, M. Loretz, C. L. Degen, *Annu. Rev. Phys. Chem.* **65**, 83–105 (2014).
20. S. Kotler, N. Akerman, Y. Glickman, R. Ozeri, *Phys. Rev. Lett.* **110**, 110503 (2013).
21. L. Jiang et al., *Science* **326**, 267–272 (2009).
22. P. Neumann et al., *Science* **329**, 542–544 (2010).
23. H. Sun, W.-Y. Chiu, J. Jiang, A. Nallanathan, H. V. Poor, *IEEE Trans. Signal Process.* **60**, 6068–6073 (2012).
24. H. J. Mamin et al., *Science* **339**, 557–560 (2013).
25. T. Staudacher et al., *Science* **339**, 561–563 (2013).
26. J. M. Cai, A. Retzker, F. Jelezko, M. B. Plenio, *Nat. Phys.* **9**, 168–173 (2013).
27. M. Mehring, *Principles of High Resolution NMR in Solids* (Springer, 2012).
28. B. Reif, *J. Magn. Reson.* **216**, 1–12 (2012).
29. S. Appelt, H. Kuhn, F. W. Hasing, B. Blumich, *Nat. Phys.* **2**, 105–109 (2006).
30. See supplementary materials.

SUPPLEMENTARY MATERIALS

www.sciencemag.org/content/356/6340/837/suppl/DC1
Materials and Methods
Supplementary Text
Figs. S1 to S5
References (*31–40*)

Editor's Summary

Enhancing quantum sensing
The quantum properties of the nitrogen vacancy (NV) defect in diamond can be used as an atomic compass needle that is sensitive to tiny variations in magnetic field. Schmitt *et al.* and Boss *et al.* successfully enhanced this sensitivity by several orders of magnitude (see the Perspective by Jordan). They applied a sequence of pulses to the NV center, the timing of which was set by and compared with a highly stable oscillator. This allowed them to measure the frequency of an oscillating magnetic field (megahertz bandwidth) with submillihertz resolution. Such enhanced precision measurement could be applied, for example, to improve nuclear magnetic resonance-based imaging protocols of single molecules.
Science, this issue p. 832, p. 837; see also p. 802

Article Tools	Visit the online version of this article to access the personalization and article tools: http://science.sciencemag.org/content/356/6340/837
Permissions	Obtain information about reproducing this article: http://www.sciencemag.org/about/permissions.dtl